G. P. Gibson, M. Capel*, and S. G. Druce**

Effect of Heat Treatment on the Fracture Toughness Transition Properties of an A508 Class 3 Steel

REFERENCE Gibson, G. P., Capel, M., and Druce, S. G., **Effect of heat treatment on the fracture toughness transition properties of an A508 class 3 steel**, *Defect Assessment in Components – Fundamentals and Applications*, ESIS/EGF9 (Edited by J. G. Blauel and K.-H. Schwalbe) 1991, Mechanical Engineering Publications, London, pp. 587–611.

ABSTRACT ASTM A508 class 3 steels undergo a transition in fracture toughness properties with temperature, due to a change in fracture mode from microvoid coalescence to cleavage fracture. We have studied the effect of heat treatment on the fracture toughness transition properties of an A508 class 3 forging. Cleavage fracture was initiated by the cracking of brittle second phase particles, primarily iron based carbides, but in a few cases titanium carbides or manganese sulphide inclusions. The critical stage in the cleavage fracture process is particle-size-dependent. For small particles (i.e. $< 1.2\ \mu m$), the critical stage is the propagation of a particle-sized microcrack into the ferritic matrix, while for larger particles the critical stage is the cracking of the particle. Decreasing the cooling rate from the austenitisation temperature from 40 to 6°C/min increased the transition temperature by 30°C due to an increase in ferritic grain size. An increase in the degree of tempering from 610°C for 5 hours to 675°C for 20 hours raised the transition temperature by 70°C due to carbide coarsening. The effect of carbide and grain size is apparently to alter the number of particles which crack and act as potential cleavage nucleation sites.

Introduction

A508 class 3 steel, in common with other ferritic steels, shows a transition in fracture toughness properties with temperature. This transition is accompanied by a change in the micromechanisms of fracture. At high temperatures, fracture occurs by microvoid coalescence which involves the formation, growth, and coalescence of voids formed around second phase particles. At temperatures below the transition temperature, final fracture occurs by cleavage along specific crystallographic planes, which renders the material relatively brittle. The transition temperature is primarily dependent on the highest temperature at which cleavage fracture occurs in a particular steel **(1)**.

The conventional heat treatment given to A508 class 3 forgings used in nuclear pressure vessel applications involves a water spray quench from the austenitisation temperature (~880°C) followed by a temper **(2)**. The average cooling rate during the quench varies through the depth of the forging and with the overall forging thickness, and can vary between 40 and 6°C/min **(3)**.

* B388, Materials Physics and Metallurgy Division, Harwell Laboratory, Oxfordshire, OX11 0RA, UK.

Tempering is normally carried out at a minimum temperature of 650°C; in practice this is generally the 'aimed for' temperature, and temperatures in the range 610–675°C are plausible, given the normal furnace tolerances for large components. There may also be additional tempering during the intermediate and final post weld heat treatment (PWHT) following the various welding operations.

The effect of quench rate and degree of tempering on the transition temperature have been studied, primarily using Charpy impact tests, on a range of low alloy pressure vessel steels, including ASTM A533B **(3)–(7)**, A508 class 2 **(8)** and 20 MnMoNi55 **(9)**. A reduction in quench rate is reported to increase the transition temperature **(3)(4)(7)** and an increase in the degree of tempering initially decreases then increases the transition temperature **(3)(5)(9)**.

Cleavage fracture in low alloy pressure vessel steels is generally triggered by the cracking of brittle second phase particles, either carbides **(1)(7)(10)–(12)** or manganese sulphide inclusions **(12)**. The cracking of these particles as a result of an impingement of a dislocation slip band, occurs at a critical shear stress (τ_c) given by equation (1) **(1)(13)**. The action of a shear stress on the dislocation slip band produces a tensile stress at the tip of the slip band which reaches the theoretical breaking strength of the particle at the critical shear stress

$$\tau_c - \tau_i = \left\{\frac{2E\gamma_p}{\pi(1-\nu^2)d}\right\}^{1/2} \tag{1}$$

where

τ_i is the lattice friction stress
γ_p is the effective surface energy of the particle
ν is Poisson's ratio
d is the grain size governing the slip band length
E is Young's Modulus

Cleavage microcracks formed by the cracking of particles propagate into the surrounding matrix at a critical effective tensile stress (σ_L) given by equation (2) **(1)(14)**.

$$\sigma_L = \left\{\frac{4E\gamma Q}{\pi(1-\nu^2)c}\right\}^{1/2} \tag{2}$$

where

$$\sigma_L = \left[\sigma^2 + \frac{\tau_e^2 d}{c}\left\{1 + \frac{4}{\pi}\left(\frac{c}{d}\right)^{1/2}\frac{\tau_i}{\tau_e}\right\}^2\right]^{1/2} \tag{3}$$

γ is the effective surface energy of the matrix

Q is a factor dependent on the ratio of particle width to thickness (w/c) **(13)(16)**
σ is the local tensile stress
τ_e is the effective shear stress, $\tau - \tau_i$

The effective tensile stress given by equation (3) comprises two components: the first is the local tensile stress; the second is a term due to the dislocation pile-up whose presence raises the level of tensile stresses in the vicinity of the microcrack. The final stage in the cleavage fracture process is the extension of the cleavage microcrack through the remaining material, and in particular across grain or bainitic packet boundaries **(17)(18)**. The critical tensile stress to propagate a grain sized microcrack into the surrounding grains is given by the Griffith equation **(1)(19)**

$$\sigma_c = \left\{\frac{4E\gamma Q}{\pi(1-\nu^2)d}\right\}^{1/2} \tag{4}$$

In this case Q is dependent on the shape of the grain.

In bainitic steels, the critical stage in the cleavage fracture process is generally the propagation of particle sized microcracks **(1)(19)**.

There are two specific aims of this study: the first is to evaluate the effect of quench rate and degree of tempering on the fracture toughness transition properties of an A508 class 3 steel; the second is to rationalise these effects in terms of the cleavage fracture mechanisms operating in these steels.

Experimental details

Material and heat treatment

The material used in this study is an A508 class 3 forging manufactured by Japan Steel Sorks. Table 1 gives the chemical composition.

Specimen blanks were cut from a block forging 1.5 m long (L) by 1.5 m wide (T) by 510 mm thick (S) prior to the subsequent heat treatments detailed in Table 2. The blanks were first given a normalisation heat treatment of 1050°C for 1 hour, to ensure the dissolution of all large iron carbides, as subsequently confirmed by transmission electron microscopy (TEM). The quench rates and tempering conditions chosen represent the likely bounds of those experienced in commercially produced forgings.

Table 1 Chemical composition wt percent

C	*Si*	*Mn*	*P*	*S*	*Cu*	*Ni*	*Cr*	*Mo*	*Al*	*As*	*Sb*	*Sn*	*V*	*Ti*
0.22	0.24	1.37	0.005	0.003	0.06	0.72	0.11	0.49	0.03	<0.01	<0.01	0.02	<0.01	7 ppm

Table 2 Heat treatment details

Normalisation	1 hr at 1050 ± 10°C air cool
Austenitisation	heat 100°C/hr to 300°C heat 30°C/hr to 880°C 10 hr at 880 ± 10°C
Quench	40°C/min to 500°C 26°C/min to 300°C or 6°C/min to 520°C 2°C/min to 300°C
Temper	heat 30°C/hr to 610°C 5 hr at 610 ± 5°C cool 18°C/hr to 300°C or heat 30°C/hr to 675°C 20 hr at 675 ± 5°C cool 18°C/hr to 300°C

Specimen details

Three types of specimens were manufactured: round tensile specimens (6.25 mm diameter and 25 mm gauge length) to a design given in ASTM E8M with their gauge lengths parallel to the longitudinal (L) orientation in the original forging; single-edge-notched, four-point bend specimens to the design shown in reference **(10)**, with their notch plane perpendicular to the longitudinal orientation and crack growth direction parallel to the through thickness orientation of the forging (L–S); and 25 mm thick plane sided compact specimens to a design based on that given in ASTM E813-87 in the L–S orientation.

Specimen testing

Tensile and single-edge-notched, four-point bend specimens were loaded at a ram displacement rate of 0.5 mm/min at one of a number of temperatures in the range −196 to +80°C and −196 to −140°C, respectively.

Compact specimens were fatigue pre-cracked to a crack length to width ratio (a/W) of approximately 0.55. Testing was carried out at a ram displacement rate of 0.5 mm/min at one temperature in the range −120 to +80°C. Specimens were loaded until they either fractured by cleavage or the applied stress intensity factor (K) derived from the J integral reached 700 MPam$^{1/2}$. In the latter cases, the specimens were unloaded, cooled and broken apart by rapid loading.

The J-integral at the onset of cleavage fracture or at specimen unloading was determined using equation (5) from the area under the load versus load-line displacement race (U) derived from the measured load versus ram displacement trace by subtracting the previously measured extraneous displacements.

$$J = \frac{\eta U}{B(W - a_0)} \left\{ 1 - \frac{(0.75\eta - 1)\,\Delta a}{(W - a_0)} \right\} \tag{5}$$

where $\eta = 2 + 0.522\,(1 - a_0/W)$

B is specimen thickness

The corresponding stress intensity factor (K) at fracture or onset of unloading was determined from equation (6), with Poisson's ratio taken as 0.3.

$$K = \left\{ \frac{EJ}{(1 - \nu^2)} \right\}^{1/2} \tag{6}$$

Results

Fractographic observations

The fracture surfaces of a number of compact, notched bend, and tensile specimens were examined in detail using a scanning electron microscope (SEM) to determine the position of the origin of cleavage fracture and the type and size of the particle initiating fracture. For all the specimens examined, there was one main nucleation site, indicated by a network of radiating major tear and river lines. In addition to the main nucleation site, there are dispersed on the fracture surface a number of 'secondary' initiation sites. These sites have been activated after a cleavage crack has initiated from the main site and are characterised by a local region of radiating river lines. Similar features were observed at both the main and secondary nucleation sites.

In nearly all the specimens examined, there was a fractured particle at the cleavage nucleation sites. In the few cases where no particle was observed, this was due to the indistinct nature of the radiating river lines close to the nucleation site, making exact location difficult. Table 3 gives a summary of the

Table 3 Details of cracked particles found at main cleavage nucleation sites

Heat treatment			*Number of observations of each particle type*		
Quench rate	*Tempering temp/time*	*Specimen geometry*	$M_{23}C_6$	*TiC*	*MnS*
40°C/min	610°C/5 h	Compact	4	2	1
		Notched bend	4	1	2
40°C/min	675°C/20 h	Compact	8	—	—
		Notched bend	8	—	—
		Tensile	1	—	—
6°C/min	610°C/5 h	Compact	8	—	—
		Notched bend	8	—	—
		Tensile	—	1	—
6°C/min	675°C/5 h	Compact	8	—	—
		Notched bend	8	—	—
		Tensile	1	—	—

types of cracked particle observed at the main nucleation sites for each of the heat treatments.

The particle most commonly found was $M_{23}C_6$ iron carbides identified from energy dispersive X-ray analysis **(20)**. The size of these particles increased with tempering being typically 0.1–0.3 μm thickness and 0.2–0.9 μm width for material tempered at 610°C for 5 hours and 0.3–1.2 μm thickness and 0.3–2.9 μm width for material tempered at 675°C for 20 hours. In addition titanium carbides of about 0.5 μm thickness and 1.4 μm width and manganese sulphide inclusions in the size range 1.5–6 μm were occasionally observed in material quenched at 40°C/min and tempered at 610°C for 5 hours. Figures 1 and 2 show examples of fractures initiated by $M_{23}C_6$ particles. The two lower fractographs in each figure are from the matching regions on the two specimens halves and clearly show that the initiating particle has itself cleaved.

Microstructural characterisation

Figure 3 shows optical micrographs of polised and etched (in 2 percent nital) sections for the four heat treatments. The faster quench rate (40°C/min) has given rise to a mainly bainitic microstructure, while the microstructure following the slower quench contains an increased proportion of ferrite. The effect of the longer tempering heat treatment (675°C for 20 hours) has been to partially spheroidise the carbides. Table 4 gives the mean ferritic grain size for each heat treatment determined as 1.5 times the mean linear intercept. The grain size is larger in material given the slower quench, but there is no effect of tempering on the grain size. The latter result suggests that the material has not been recrystallised even after the longer tempering heat treatment.

Carbon extraction replicas, examined in TEM, were used to determine the particle thickness (c) distributions arising from the heat treatments. About 2000 individual particles were assessed for each condition. The measured area particle thickness distributions [$N_a(c)$] were converted to true or volumetric distributions [$N_v(c)$] using equation (7) **(21)**.

$$N_v(c)dc = \frac{N_a(c)dc}{c(W/c)_a} \tag{7}$$

where $(W/c)_a$ is the average width to thickness ratio of the particles and $c(W/c)_a$ the assumed distance below the specimen surface from which particles are extracted. Figure 4 shows the normalised volumetric particle thickness distributions for each of the four heat treatments, for particles thicker than 0.022 and 0.05 μm for the short and long tempering heat treatments respectively. The volumetric distributions were fitted to a simple exponential function given by equation (8). The values of the coefficients A and B are given in Table 4.

$$N_v(c) = Ae^{-BC} \tag{8}$$

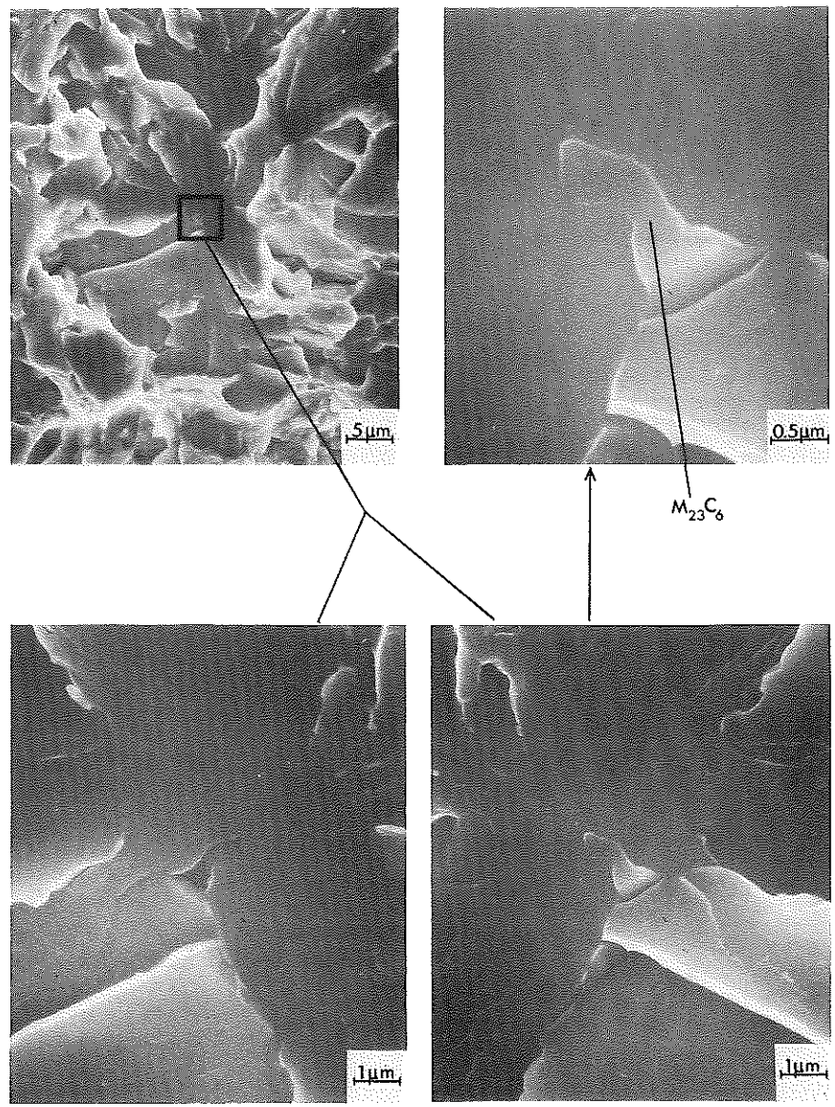

Fig 1 Fractographs showing cracked iron carbide at main nucleation site in material, quenched 6°C/min and tempered 675°C for 20 hours

The thickness of the particles is considerably greater following the longer tempering treatment. In addition, the particle distributions are similar for the two quench rates, except that there is a slightly higher proportion of larger particles in the slower quenched materials. The number of iron carbides in

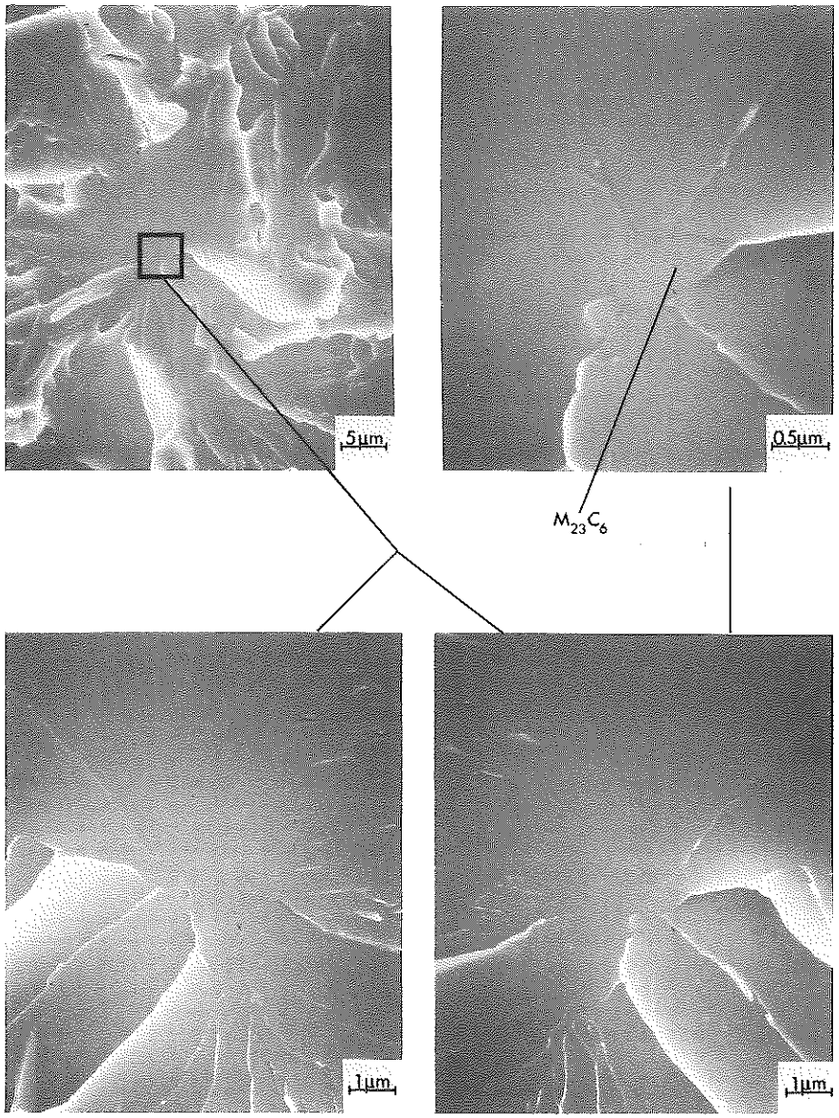

Fig 2 Fractographs showing cracked iron carbide at main nucleation site in material, quenched 40°C/min and tempered 675°C for 20 hours

each size range observed at the main nucleation sites are also given in Fig. 4. The carbide particles which nucleate fracture represent the coarser particles found in the microstructure, for all testing temperatures investigated (−196–+80°C).

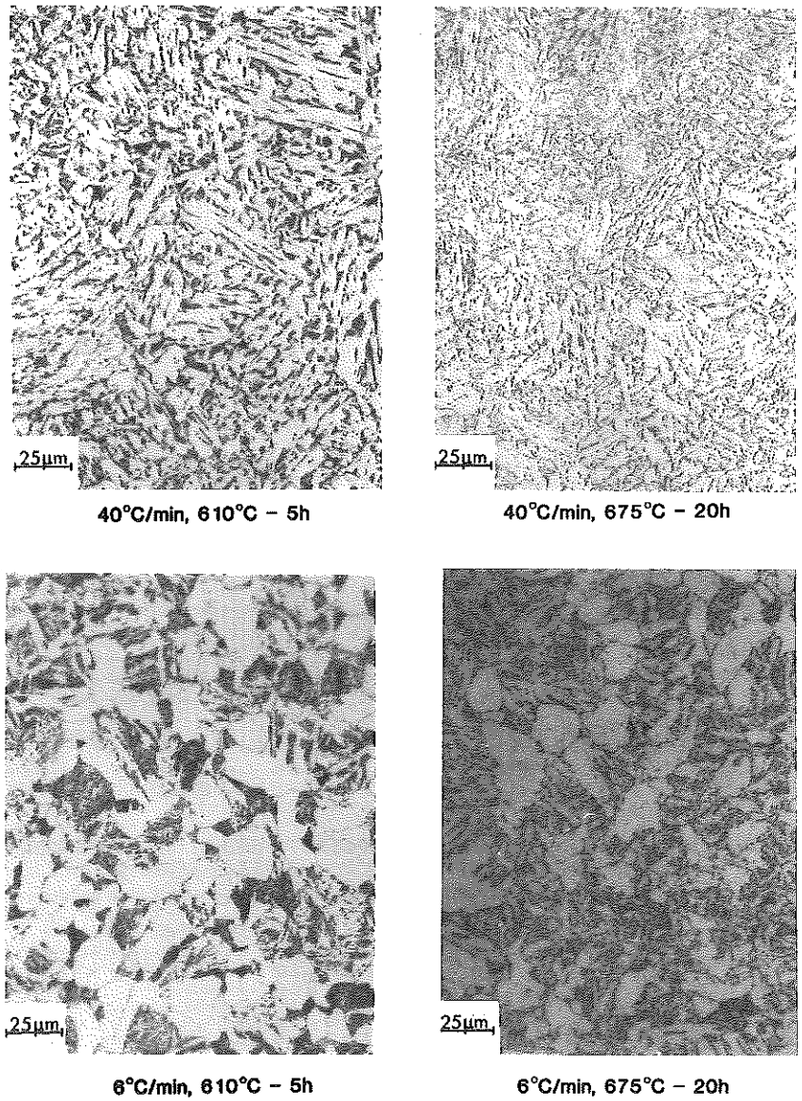

Fig 3 Optical micrographs of polished and etched sections for the four heat treatments

Tensile results

Figure 5 shows the effect of temperature on the 0.2 percent proof stress ($\sigma_{0.2}$) and ultimate tensile stress (σ_t) for material tempered at 610°C for 5 hours or 675°C for 20 hours, following a quench at 40 or 6°C/min. In each case, the proof and ultimate tensile stress decrease with increasing temperature, particu-

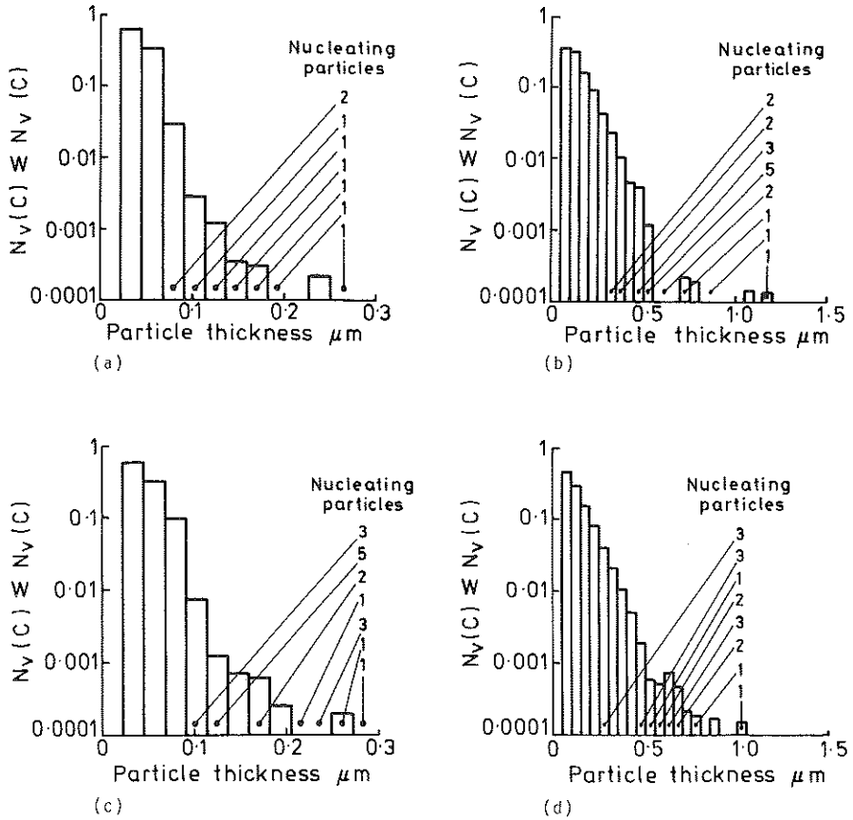

Fig 4 Normalised volumetric particle thickness distributions for material (a) quenched 40°C/min and tempered 610°C for 5 hours; (b) quenched 40°C/min and tempered 675°C for 5 hours; (c) quenched 6°C/min and tempered 610°C for 5 hours; (d) quenched 6°C/min and tempered 675°C for 20 hours

Table 4 Grain size and particle thickness distributions

Heat treatment			*Coefficients of particle thickness distribution*	
Cooling rate	*Tempering temperature and time*	*Grain size ± standard error μm*	*A* μm^{-3}	*B* μm^{-1}
40°C/min	610°C–5 h	4.7 ± 0.3	54 000	71
40°C/min	675°C–20 h	4.6 ± 0.2	350	14
6°C/min	610°C–5 h	9.5 ± 0.3	15 000	58
6°C/min	675°C–20 h	9.4 ± 0.4	63	13

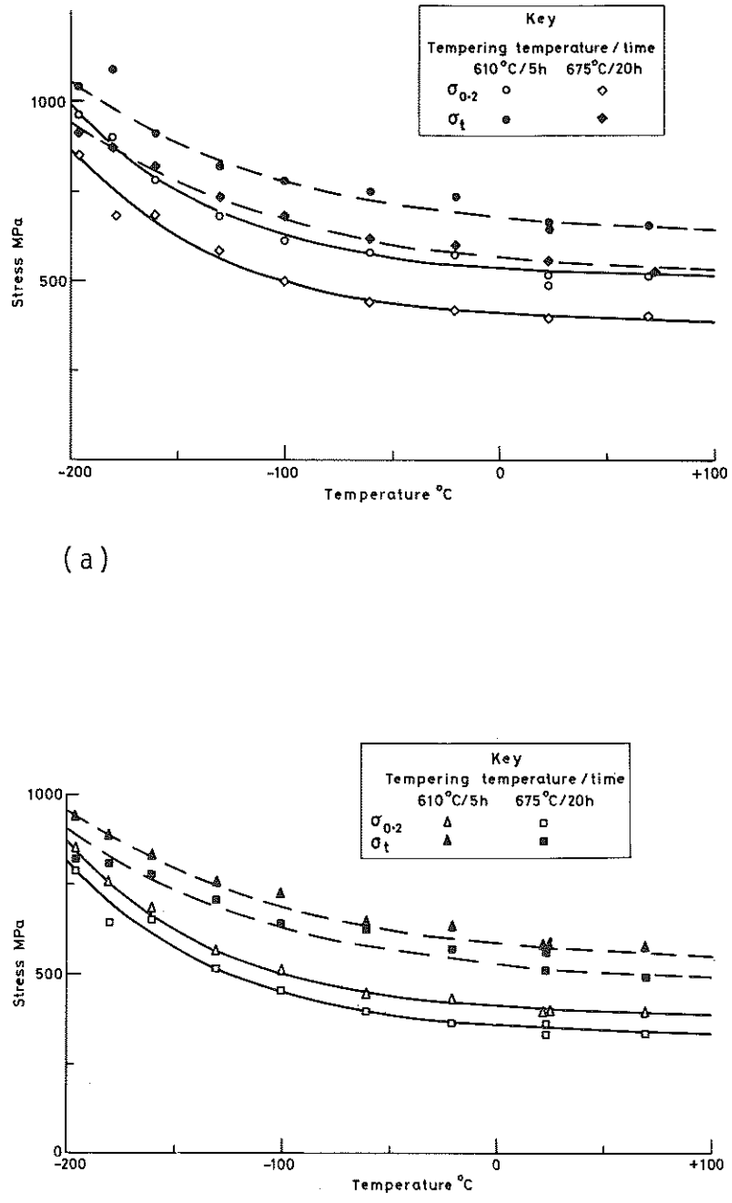

Fig 5 Effect of temperature on proof and tensile stress for material quenched at (a) 40°C/min and (b) 6°C/min

larly at low temperatures. The proof and ultimate tensile stresses are lower for material quenched at the slower rate, which is probably mainly due to the larger ferritic grain size, see Table 4. The effect of increased tempering is also to lower the proof and ultimate tensile stress, probably due to dislocation recovery and particle coarsening. The tensile data were used to calculate the variation with temperature of Young's modulus, strain hardening and reference stress **(22)**.

Notched bend and fracture toughness results

The stresses generated in blunt-notched and sharply cracked specimens vary with distance ahead of the notch or crack **(23)–(28)**. In blunt notched specimens the peak tensile stress occurs ahead of the notch tip and both the distance ahead of the notch and magnitude of the peak tensile stress increase with specimen loading. The shear stresses are highest at the notch tip and also increase with specimen loading. The tensile stress distribution generated ahead of a stationary sharp crack shows a peak value located ahead of the crack tip at a distance (Xp) which increases linearly with K^2. The peak shear stress is generated at the crack tip. Both tensile and shear stress distributions ahead of sharp cracks are independent of the level of K when the distance ahead of the crack tip is normalised by $(K/\sigma_r)^2$, but are dependent on the reference stress (σ_r), work hardening exponent and Young's modulus. The stress distributions

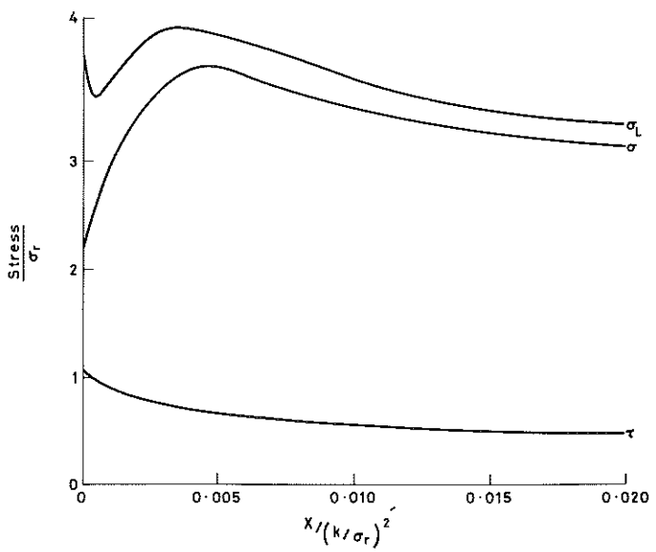

Fig 6 Shear (τ), tensile (σ) and effective tensile stress (σ_L) distributions ahead of a sharp crack for a material with a work hardening exponent of 0.1 and a reference stress to Young's modulus ratio of 1/300

ahead of the crack tip after some amount of ductile crack growth will be approximately the same as those generated ahead of stationary cracks provided J uniquely describes the crack tip conditions **(26)**.

The effective tensile stress distribution in both blunt notched and sharply cracked specimens (equation (3)) is dependent on the tensile and shear stress distributions, the particle size, grain size, and lattice friction stress. As an example, Fig. 6 shows the effective tensile stress to reference stress ratio as a function of normalised distance ahead of a sharp crack for a particle size of 0.57 μm, a grain size of 4.6 μm and lattice friction stress to reference stress ratio of 0.13, typical for a material given a 40°C/min quench and a temper at 675°C for 20 hours. Effective tensile stress values are higher than the tensile stress values, and the peak effective tensile stress occurs closer to the crack tip than the peak tensile stress value.

Fractographic examination of broken specimens allows the position of the main nucleation site ahead of the notch tip (X_c) to be determined. Comparison of the relative positions of the main nucleation site and the peak tensile stress (X_p) can indicate which type of stress (i.e. shear, effective tensile or tensile) is critical for cleavage fracture and thus the critical stage in the cleavage fracture process, as each of the stages in the cleavage fracture process involves a different type of stress, see above. Figures 7 and 8 show X_c/X_p data as a function of test temperature for the various heat treatments tested using blunt notched and sharp cracked specimens, respectively.

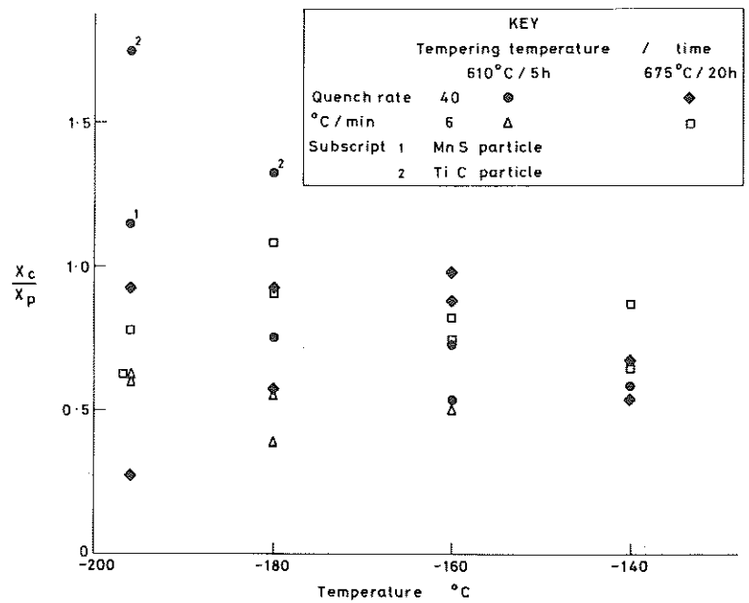

Fig 7 Effect of temperature on X_c/X_p ratio in notched bend specimens for the four heat treatments

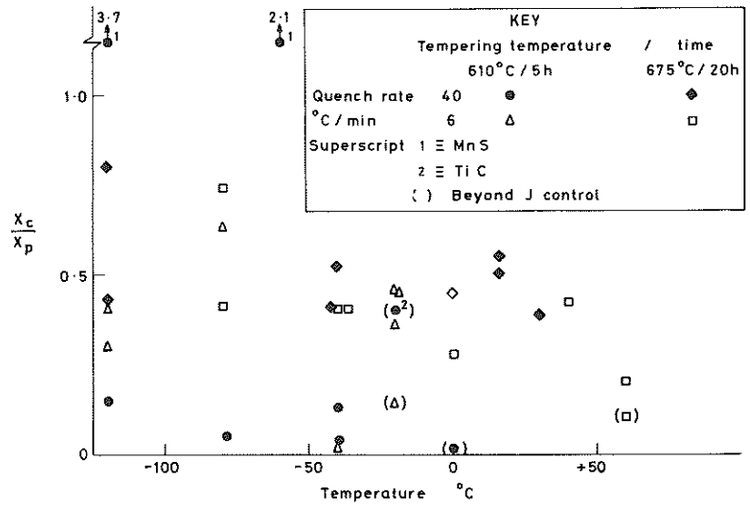

Fig 8 Effect of temperature on X_c/X_p ratio in compact specimens for the four heat treatments

In cases where iron carbides were found at the main nucleation sites (non-subscript points) the X_c/X_p ratio is above zero but less than unity. Therefore, in these cases the main nucleation sites are located close to the peak effective tensile stress, suggesting that the propagation of particle sized microcracks is the critical stage. It is worth noting that for compact specimens when the X_c/X_p ratio is less than unity, the level of the tensile stress at the nucleation site was decreasing with increasing loading at the latter stages of loading prior to fracture. The X_c/X_p ratio when fracture is nucleated by the cracking of manganese sulphide inclusions in compact specimens or manganese sulphide or titanium carbide particles in blunt notch specimens is significantly greater than unity. In these cases, it is not possible to ascertain the type of stress controlling fracture from the X_c/X_p results but the level of the shear, tensile or effective tensile stress at the initiation site for fracture will be less than the peak values.

Comparison of Figs 7 and 8 shows a higher proportion of fracture initiation sites at low values of X_c/X_p in sharp cracked specimens as compared with blunt notched test pieces. In both geometries low values of X_c/X_p are associated with small particles resulting from the shorter tempering treatments. This can be understood with reference to equation (3), where the shear stress contribution to the effective tensile stress is more dominant with decreasing particle size. In sharp cracked specimens this effect is more pronounced as the levels of shear stress close to the crack tip are higher than found in blunt-notched specimens.

In cases where the critical stage of the cleavage fracture process is the propagation of particle sized microcracks, the effective tensile stress at fracture

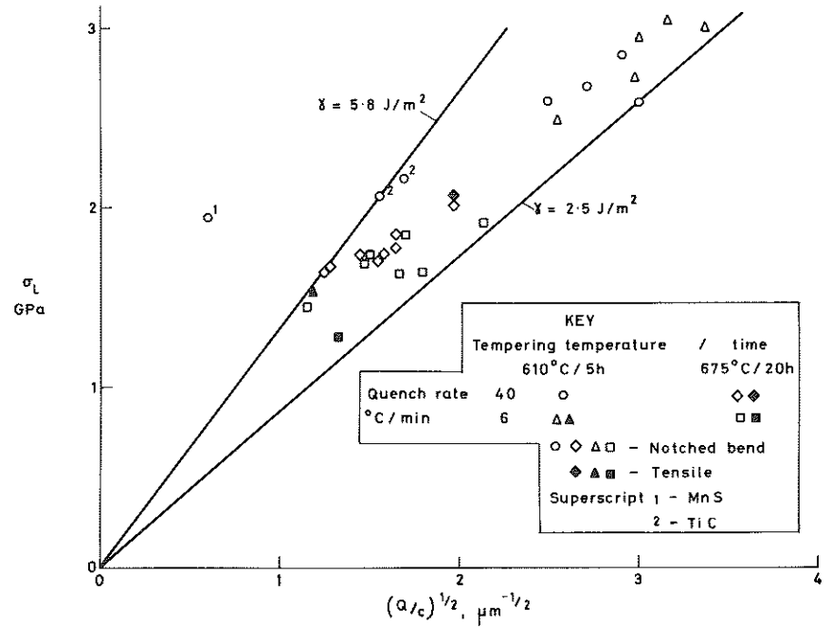

Fig 9 Effective tensile stress versus $(Q/c)^{1/2}$ in notched bend and tensile specimens for the four heat treatments

should be inversely dependent on the particle size, see equation (2). Figures 9 and 10 show the effective tensile stress at fracture versus $(Q/c)^{1/2}$ for the notched bend specimens and tensile specimens (tested at −196°C), and for compact specimens respectively. The effective tensile stress was determined using equation (3) from the tensile and shear stresses at the nucleation site as determined from the notch and crack tip stress distributions **(23)(24)**, the cracked particle dimensions measured from the fracture surface, the grain size given in Table 4 and the lattice friction stress (τ_i) determined from the Hall-Petch **(27)(28)** equation, assuming a Tresca yield criterion.

$$\sigma_{0.2} = 2\tau_i + k_y d^{1/2} \tag{9}$$

where k_y the Hall-Petch coefficient, was taken as 0.55 MN/m$^{1.5}$ **(29)**.

It can be seen from Figs 9 and 10 that there is a reasonably linear relationship between the critical effective tensile stress values at fracture and $(Q/c)^{1/2}$ in cases of iron based carbide nucleated fracture. In addition, the results for titanium carbide nucleated fracture are consistent with those for iron carbide nucleated fracture. Therefore, this suggests that the propagation of particle sized microcracks is the critical stage in these cases, see equation (2). In addition, values of the effective surface energy for the ferritic matrix (γ) determined from equation (2) taking Young's modulus as 214 GPa and Poisson's ratio as

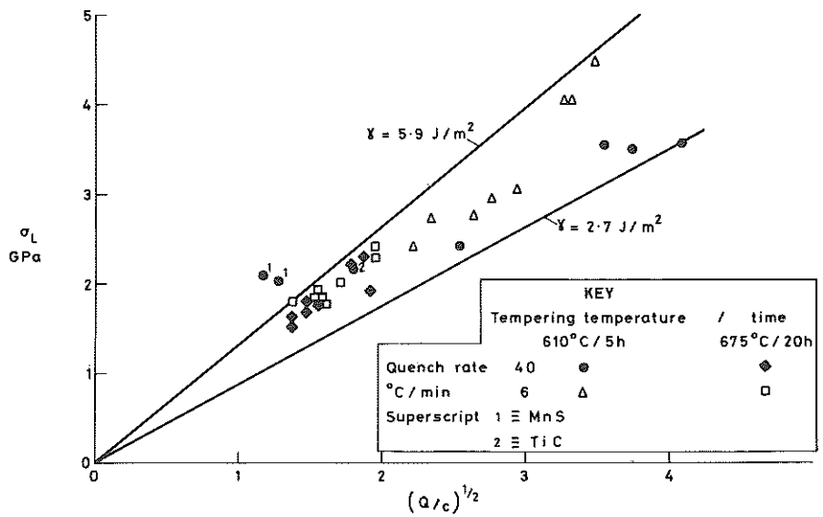

Fig 10 Effective tensile stress versus $(Q/c)^{1/2}$ in compact specimens for the four heat treatments

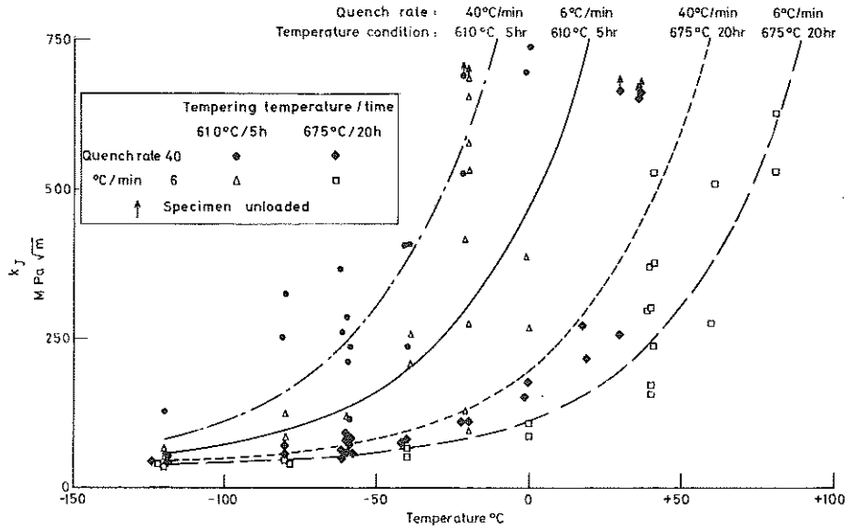

Fig 11 Effect of temperature on fracture toughness for the four heat treatments

0.3, are between 2.5 and 5.9 J/m^2, within the range reported for other ferritic steels of 2 to 21 J/m^2 **(1)**. The range of γ values determined (2.5–5.9 J/m^2) include cases where fracture is initiated from iron and titanium carbides in tensile, notched bend, and compact specimens. Both the size of initiating particles and the critical effective tensile stress were found to be only weakly dependent on test temperature.

The effective tensile stress values in the cases where fracture was nucleated from manganese sulphide inclusions is higher than those predicted from the carbide results. This occurs because the values of the effective tensile stress within the plastic zone are more than sufficient to propagate microcracks formed in the larger manganese sulphide inclusions and therefore this is no longer the critical stage. Furthermore, the critical stage is not the propagation of grain sized microcracks because the tensile stress, which equals the effective tensile stress in the case of large particles, will be more than sufficient to propagate grain sized microcracks as the grain size exceeds the particle size. Therefore, the critical stage is the cracking of the particle in these cases. Consistent with this conclusion is the fact that the values of the effective surface energy for manganese sulphide derived from the shear stress at fracture using equation (1) are between 0.6 and 1.1 J/m^2, and hence less than that determined from the ferritic matrix. This is a necessary condition for particles to act as brittle cleavage nucleation sites.

Figure 11 shows the effect of temperature on fracture toughness (K_J) measured from compact specimens, for the four heat treatments. These data have been analysed using multilinear regression to determine the effect of heat treatment on the transition toughness properties. A wide range of equations were fitted to the data: the most accurate was found to be equation (10)

$$\ln (K_J - 35 \text{ MPa}\sqrt{\text{m}}) = A + B \times QR + C \times TC + D \times T \qquad (10)$$

where

A, B, C, D are fitted coefficients ($A = 5.58$, $B = -0.761$, $C = 1.76$, $D = 0.0252$)
T is temperature in °C
QR is the quench rate coefficient (-0.5 if 6°C/min, 0.5 if 40°C/min)
TC is the tempering treatment coefficient (-0.5 if 675°C for 20 hours and 0.5 if 610°C for 5 hours).

Higher order terms of temperature, quench rate and degree of tempering such as T^2, $QR \times T$, and $TC \times T$ were found to be not statistically significant at the 95 percent confidence level. The toughness–temperature relationships predicted from equation (10) are given in Fig. 11. It can be seen that equation (10) gives a reasonable fit to the data over a wide range of toughness values. Equation (10) suggests that the shift in toughness properties with changes in quench rate and degree of tempering is uniquely defined and not inter-related or dependent on temperature. Similarly, the shift in the transition temperature (defined as the temperature for a given level of toughness) due to changes in quench rate or degree of tempering is uniquely defined. The increase in transition temperature ($\pm$ standard error) due to an increase in the degree of tempering from 610°C for 5 hours to 675°C for 20 hours is 70 $\pm$ 5°C. A decrease

Table 5 99 percent percentile particle sizes (μm)

		Tempering temperature (°C)/time (h)	
		610/5	*675/20*
Quench rate (°C/min)	6	0.079	0.354
	40	0.065	0.329

Coefficients (mean $\pm$ standard error) in transition temperature to grain and particle size relationship (equation (12))

$F = -173.72 \pm 0.03$°C

$G = 27.17 \pm 0.01$°C/μm$^{1/2}$

$H = 221.40 \pm 0.03$°C/μm$^{1/2}$

in quench rate from 40° to 6°C/min increases the transition temperature ($\pm$ standard error) by 30 $\pm$ 5°C.

Effect of temperature on effective surface energy

Figure 12 shows the effect of temperature on the effective surface energy for the ferritic matrix determined using equation (2) from the effective tensile stress and particle sizes at fracture measured in compact, notched bend, and tensile specimens in cases where fracture was nucleated by iron or titanium carbides. Similar results were obtained for material generated at 6°C/min. The effective surface energy is independent of temperature in the range -196 to $+60$°C. In addition, there is little or no effect of test specimen geometry, particle type, (i.e., iron or titanium carbide) or heat treatment on the effective surface energy.

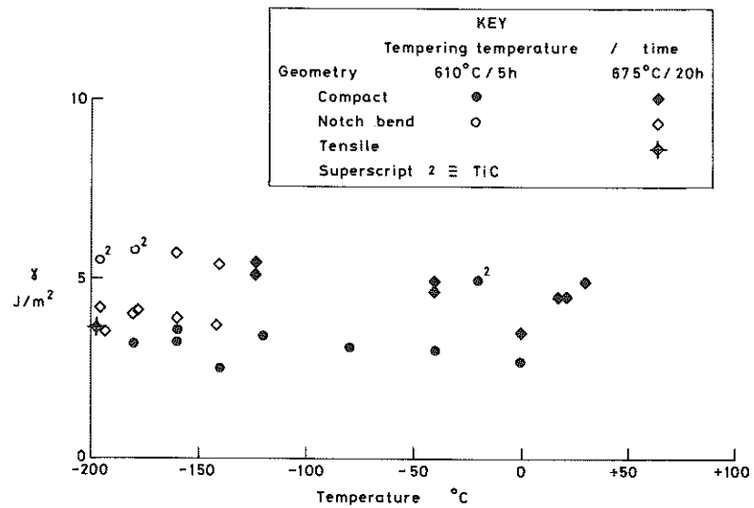

Fig 12 Effect of temperature on effective surface energy for ferritic matrix for material quenched at 40°C/min

Discussion

Cleavage initiating particles and the cleavage fracture mechanism

Fractographic observations of broken specimens show that for the material in this study, cleavage fracture is initiated by the cracking of brittle second phase particles, primarily iron based carbides, see Table 3. The importance of carbides in the cleavage fracture mechanism of quenched and tempered bainitic and martensitic steels has been noted by a number of authors **(1)(7)(10)–(12)(30)(31)**. Naylor and Guttman **(7)** observed that secondary cleavage cracks below the fracture surface had apparently initiated from iron carbides of the type found in this study ($M_{23}C_6$). In addition Bowen *et al.* **(10)** showed a link between the coarsest carbide size located in the microstructure and the peak tensile stress at fracture measured in notched bend specimens. Further analysis of their data reveals a better link between coarsest carbide size and peak effective tensile stress at fracture **(1)**.

Observations that titanium carbides can initiate fracture in quenched and tempered bainitic steels has not apparently been reported previously. However, Lewandowski and Thompson **(32)** have observed that Ti (C, S) inclusions can initiate fracture in pearlitic steels. In the present study, titanium carbides were only observed to initiate fracture in material given the shorter tempering treatment (610°C for 5 hours). The explanation for this is due to a change in the relative size of the titanium and iron carbides with tempering. Titanium carbides could not be dissolved by the initial 1050°C heat treatment and would therefore be present prior to subsequent tempering treatments. In material given a short tempering treatment, the coarsest iron carbides (0.2 to 0.3 μm) are smaller than the titanium carbides (0.5 μm). In these cases, the titanium carbides are relatively potent cleavage nucleation sites because the required effective tensile stress values to initiate fracture is lower (see equation (2)) and consequently they are occasionally observed to initiate cleavage fracture, even though they have a much lower population density than the carbides, due to the low titanium content of the steel, see Table 1. In material given the long tempering treatment (675°C for 20 hours), the coarsest iron carbides (1 to 1.2 μm) will be larger than the titanium carbides. The titanium carbides will not coarsen significantly with tempering because of the large distances between these sparsely populated particles over which diffusion of chemical species has to occur. Therefore, in these cases, the titanium carbides are no longer relatively potent cleavage nucleation sites and consequently would not be expected to initiate cleavage fracture.

The only other type of particle observed to nucleate fracture in this study were manganese sulphide inclusions, see Table 3. Manganese sulphide inclusions have also been observed by Rosenfield *et al.* **(12)(30)** to initiate cleavage fracture in quenched and tempered bainitic steels. Their evidence suggested that cleavage fracture from manganese sulphide inclusions was particularly prevalent at temperatures corresponding to the upper transition regime **(30)**.

However, this suggestion is not supported by the results in this study, which show that manganese sulphide initiated fracture was apparently limited to temperatures corresponding to the lower shelf regime, see Figs 7 and 8. The observations of manganese sulphide initiated fracture are perhaps surprising, given that manganese sulphide has a higher thermal expansion coefficient than steel **(33)**. Consequently, on cooling the steel from the hot working temperature, a stress distribution is set up in and around the inclusion trying to debond the inclusion from the matrix; in such a case the inclusion could no longer crack and act as a cleavage nucleation site. However, the larger size of the inclusions relative to the carbides does make them potent cleavage nucleation sites if they can be made to fracture. This is particularly the case for material given the shorter tempering treatment and faster quench (compared in Figs 7–11), which probably explains why manganese sulphide initiated fracture is apparently limited to material given this heat treatment, see Table 3.

The values for the effective surface energy for the ferritic matrix (γ) were found to fall in a relatively narrow band between 2.5–5.9 J/m^2 and within the range reported for other bainitic steels of 2–12 J/m^2 **(1)**. The lower variability of γ found in this study is primarily due to the fact that the values of γ in this study were calculated from known sizes of particles which initiated fracture, whereas those reported in reference **(1)** were generally obtained assuming that the coarsest or near coarsest particle (typically carbides) observed in the microstructure initiated fracture. The results of this study show that this is not always a reasonable assumption, see Fig. 4.

The γ values calculated in this study are apparently independent of heat treatment, see Figs 9 and 10, consistent with the results in reference **(1)** which reported similar γ values for a wide range of ferritic steels, including low carbon, mild, spheroidised, pearlitic, bainitic and martensitic steels, as well as weld metals.

γ was found to be independent of temperature over the whole measured range of -196 to $+60$°C, which spans the lower shelf and the transition regime, see Figs 11 and 12. The experimental evidence on ferritic steels in the literature also supports the conclusion that γ is basically temperature independent **(1)**. Tetelman **(34)**, following a theoretical analysis, suggested that γ would increases with increasing temperature due to additional dislocation motion during crack propagation. However, provided the cleavage propagation rate is high, the effect of temperature is predicted to be very small over the temperature range of interest (-200 to $+100$°C). The effect of temperature on γ reported by Wallin *et al.* **(35)** arises from an attempt to model the rapid increase in fracture toughness properties in the transition regime from a knowledge of the mechanisms of cleavage fracture. In the model, fracture toughness is predicted from the known crack tip stress distributions and the particle size distribution using equation (2), but neglecting the shear stress term when calculating the effective tensile stress. In order to predict the rapid increase in transition toughness properties using the model, γ had to be highly temperature dependent. The results of this study show that this assumption is incorrect, as γ is approximately independent of temperature even in the transition regime. An alternative explanation of the rapid increase in transition toughness properties with temperature is discussed below.

Another important assumption in the model of Wallin *et al.* **(35)** is that only a proportion of the particles present in the microstructure can be considered as potential nucleation sites (i.e. an eligibility factor) and that this proportion is independent of temperature. The eligibility factor is the probability that a particle will crack in a region where the effective tensile stress is sufficient to propagate a particle sized microcrack. Using an eligibility factor avoids the need to model the occurrences of particle cracking in the plastic zone around the crack tip, which would require a knowledge of the number of particles of each size which crack as a function of shear stress and the factors affecting this relationship. To ascertain whether the eligibility factor is temperature independent, the results of this study have been used to determine approximate estimates for the eligibility factor. The eligibility factor was determined from the inverse of the number of particles of size equal or greater than that which initiated fracture, which were subjected to an effective tensile stress equal to that at fracture. This in turn was determined from the number of particles per unit volume with a size equal to or greater than that observed on the fracture surface obtained from the particle size distribution (equation (8)), and the volume of material subjected to an effective tensile stress equal to that at fracture. The latter, as a first approximation, is given by equation (11).

$$\text{Volume subjected to effective tensile stress for fracture} = \text{Specimen thickness} \times (X_c + \Delta a)^2 \quad (11)$$

where $X_c + \Delta a$, the distance from the original crack tip to the nucleation sites, is the distance ahead of the original crack tip in which material was subjected to an effective tensile stress equal to that at fracture, at some stage during specimen loading, see above. Figure 13 shows a plot of the eligibility factor versus temperature, referenced to the temperature corresponding to a toughness of 250 MPa$\sqrt{\text{m}}$ obtained from equation (10) for the four heat treatments. The eligibility factor decreases with increasing temperature, showing that there is a reduction in the proportion of particles which crack as the temperature increases. There is some evidence to support this observation. McMahon and Cohen **(36)** observed that the number of cleavage microcracks arising from cracked carbides in a plain carbon steel decreased with increasing temperature at a given level of strain in tensile specimens. Therefore, it would appear that the rapid increase in fracture toughness properties in the transition regime is due to a reduction in the eligibility factor rather than a change in γ.

The effect of temperature on the eligibility factor, and thus the proportion of particles which crack, can be understood by considering the mechanism of

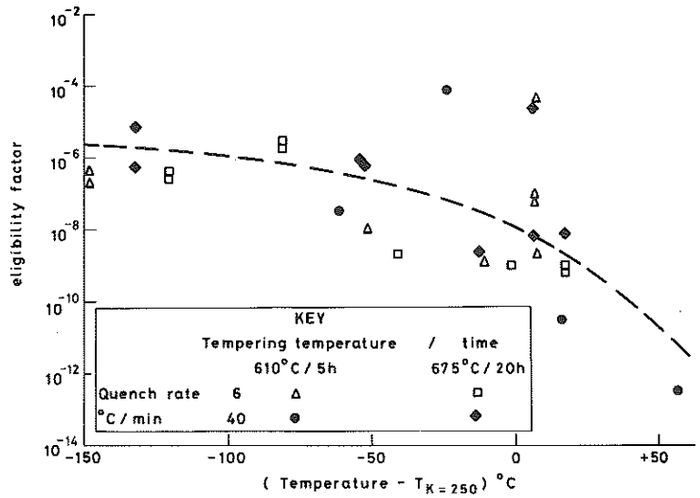

Fig 13 Eligibility factor versus temperature relative to that for a toughness of 250 MPa$\sqrt{m}$

particle cracking. Particle cracking results from the very high tensile stresses generated ahead of a blocked dislocation slip band acted upon by a shear stress. However, as the temperature increases, dislocation cross slip and climb becomes more prevalent and these can relieve the tensile stresses which are generated, and so inhibit the particle cracking. Therefore, as the temperature increases, there will be proportionately fewer particles which crack. There are two factors which are likely to affect the temperature at which there is a significant reduction in the number of particles which crack, and thus the transition temperature; the first is particle size because it will be more difficult for a dislocation to cross slip or climb around a larger particle; the second is grain size, as increasing grain size increases the length of the dislocation slip band, which in turn increases the stresses generated at the tip of a blocked slip band **(37)**, and thus the likelihood of sufficient stresses being generated to crack the particle. Therefore, the transition temperature, defined in this instance as the temperature corresponding to a toughness of 250 MPa$\sqrt{m}$ as determined from equation (10) ($T_{K=250}$) should be related to grain size and particle size. As cleavage fracture is principally initiated from the larger iron carbide particles found in the microstructure, the appropriate particle size to relate to transition temperature is considered to be that corresponding to the 99 percent percentile (C_{99}), as determined from the particle size distributions given by equation (8). Table 5 gives the values for C_{99}. The large manganese sulphide inclusions observed to nucleate cleavage fracture in material quenched at 40°C/min and tempered at 610°C for 5 hours, did so only infrequently and only at relatively low temperatures. Consequently, the mean transition temperature for this material is governed by the carbide size rather than the inclusion size. The

transition temperature was related to grain and particle size using equation (12).

$$T_{K=250} = F + G \times d^{1/2} + H \times C_{99}^{1/2} \quad (12)$$

The square root dependence of grain size follows from the fact that the stresses generated ahead of a blocked slip band are proportional to the square root of the slip band length and thus the grain size **(37)**. The square root dependence of carbide size follows a suggestion by Mintz **(38)**. The coefficients F, G, and H were determined by multi-linear regression, and their mean and standard errors are given in Table 5. The standard error values are relatively small as the fit to the data was very good, with the regression coefficient being 0.99999998. Other possible dependence of grain size and particle size on transition temperature were investigated, but the fit to the data was never as good as with equation (12). Equations (12) and (10) can be combined to give equation (13) which relates the toughness–temperature relationship to grain and particle size.

$$\ln (K_j - 35 \text{ MPa}\sqrt{m}) = 9.75 + 0.00252 \times T - 0.685 \times d^{1/2} - 5.58 \times C_{99}^{1/2} \quad (13)$$

Equations (12) and (13) have been determined for one cast of A508 class 3 steel. Further work on other pressure vessel steels is in hand to determine whether these equations have wider applicability.

Conclusions

(1) Decreasing the quench rate in an ASTM A508 class 3 steel forging from 40 to 6°C/min raised the transition temperature by 30 ± 5°C (mean ± standard error). The effect of quench rate was primarily due to a change in the ferritic grain size. There was little effect on carbide sizes.

(2) Increasing the degree of tempering from 5 hours at 610°C, to 20 hours at 675°C raised the transition temperature by 70 ± 5°C (mean standard error). The effect of tempering was due to an increase in carbide size.

(3) Cleavage fracture was initiated by the cracking of particles, primarily iron based carbides ($M_{23}C_6$ type), but occasional titanium carbides and manganese sulphide inclusions. The critical stage in the cleavage fracture process was dependent on particle size. In the case of the iron and titanium carbides, all smaller than 1.2 μm, the propagation of particle sized microcracks into the ferritic matrix was the critical stage. For the manganese sulphide inclusions observed to nucleate fracture, all larger than 1.5 μm, the cracking of the particle was the critical stage.

(4) The effective surface energy for cleavage propagation in a ferritic matrix (γ) was in the range 2.5 to 5.9 J/m^2. γ was independent on test specimen geometry (plain tensile, blunt notched four-point bend, and fatigue cracked compact specimen) and particle type (iron or titanium carbide). There was

no effect of temperature on γ in the range -196 to $+60$°C and consequently this does not explain the sharp increase in fracture toughness properties in the transition regime.

(5) The sharp increase in toughness in the transition regime is apparently due to a reduction in the number of particles which crack and act as potential cleavage nucleation sites. Increases in particle size and grain size raise the transition temperature probably due to an effect on the number of cracked particles.

Acknowledgement

This work was partly funded by the CEGB as part of the Thermal Reactor Agreement.

References

(1) GIBSON, G. P. (1988) Review of cleavage fracture mechanisms in ferritic steels, *UKAEA Report* **R13227**.
(2) ASME, Specification for Quenched and tempered vacuum-treated carbon and alloy steel forgings for pressure vessels, SA-**508**.
(3) MIYANO, K. *et al.* (1971) On the heat treatment, microstructure and mechanicsl properties of heavy gauge steels for nuclear pressure vessels, *Japan Steel Works Technical News.* **2**, 10–19.
(4) KUNITAKE, H., NAKAO, H., KIKUTAKE, T., SAITO, A., ISHIGURO, T., and TAKEDA, T. (1977) 3rd Int. conf. on pressure vessel technology, *ASME*, pp. 603–611.
(5) ENAMI, T., SATO, S., TANKA, T., and FUNAKASHI, T. (1974) Effect of cooling rates and tempering conditions on the strength and toughness of Mn-Ni-Mo, Cr-Mo steel plate, *Kawasaki Steel Technical Report*, **6**, 1–16.
(6) LOGSDON, W. A. (1982) *J. Mater. Energy Systems*, **3**, 39–50.
(7) NAYLOR, J. P. and GUTTMANN, M. (1981) *Met. Sci.*, **15**, 433–441.
(8) CURRY, D. A. (1984) The influence of heat treatment on the cleavage fracture toughness of A508 class 2 pressure vessels steel, TPRD/L/2592/N83, CEGB, Leatherhead, Surrey.
(9) FORSCH, K., PIEHL, K-H., and WITTE, W. (1985) Effect on the precipitation condition of the carbide phases on the fracture toughness properties of heavy forgings from steel grade 20MnMoNi55, *Thyseen Technische Berichte*, **1**, 34–41.
(10) BOWEN, P., DRUCE, S. G., and KNOTT, J. F. (1986) *Acta Met.*, **34**, 1121–1131.
(11) IRWIN, G. R. (1986) Brittle–ductile transition behaviour in reactor vessel steels, Presented at a WRSI meeting, NBS-Gaithersburg, USA.
(12) ROSENFIELD, A. R., SHETTY, D. K., and SKIDMORE, A. J. (1983) *Met. Trans*, **14A**, 1934–1937.
(13) SMITH, E. and BARNBY, J. T. (1967) *Met. Sci. J.*, **1**, 56–64.
(14) SMITH, E. (1966) Physical basis of yield and fracture, Conference proceedings, Inst. Phys. and Phys. Soc., London, 36–46.
(15) IRWIN, G. R. (1962) *J. Appl. Mech.*, **29**, 651–654.
(16) VEISTINEN, M. K. and LINDROOS, V. K. (1984) Application of fracture mechanics to materials and structures, (Edited by G. C. Shih, *et al.*), pp. 377–391.
(17) BROZZO, P., BUZZICHELLI, G., MASCANZONI, A., and MIRABILE, M. (1977) *Met. Sci.*, **11**, 123–129.
(18) KOTILAINEN, H. (1980) *Fracture and Fatigue, Elasto-plasticity. Thin Sheet and Micromechanisms Problems*, (Edited by J. C. Radon), Pergamon Press, Oxford, pp. 217–226.
(19) GRIFFITH, A. A. (1921) *Phil. Trans. R. Soc. Lond., A*, **221A**, 163–198.
(20) DRUCE, S. G., TITCHMARSH, J. M., JORDAN, G., and JAMES, A. (1985) Metallurgical observations of a French A508 class 3 forging with respect to transition toughness behaviour, *UKAEA Report* **R11626**.

(21) ASHBY, M. F. and EBELING, R. (1966) *Trans AIME*, **236**, 1396–1404.
(22) CORNEC, A. and HEERENS, J. (1985) Procedure for the determination of a theoretical blunting line, presented at the CSNI Workshop on Ductile fracture test methods, Paris.
(23) GRIFFITHS, J. R. and OWEN, D. R. J. (1971) *J. Mech. Phys Solids*, **19**, 419–431.
(24) WALL, M. (1988) private communication.
(25) McMEEKING, R. M. (1977) *J. Mech. Phys Solids*, **25**, 357–381.
(26) RICE, J. R., DRUGAN, W. J., and SHAM, T-L. (1980) *ASTM STP 700*, ASTM, Philadelphia, pp. 189–221.
(27) HALL, E. O. (1951) *Proc. Phys. Soc. Lond., Ser. B*, **64**, 747–753.
(28) PETCH, N. J. (1953) JISI, **174**, 25–28.
(29) PICKERING, F. B. (1978) *Physical metallurgy and the design of steels, Applied Science*, publishers, London.
(30) ROSENFIELD, A. R. and SHETTY, D. K. (1986) *Scripta Met.*, **20**, 439–440.
(31) EHL, W., MUNZ, D., and BRÜCKNER, A. (1986) Proc. 6th European Conference on Fracture, Amsterdam. Engineering Materials Advisory Services, pp. 577–589.
(32) LEWANDOWSKI, J. J. and THOMPSON, A. W. (1986) *Met. Trans*, **17A**, 1769–1786.
(33) BROCKSBANK, D. and ANDREWS, K. W. (1972) *JISI*, **210**, 246–255.
(34) TETELMAN, A. S. (1962) *AIME Conference No* **20**, AIME, pp. 461–501.
(35) WALLIN, K., SAARIO, T. and TÖRRÖNEN, K. (1987) *Int. J. Fracture*, **32**, 201–209.
(36) McMAHON, C. J. Jr, and COHEN, M. (1955) *Acta Met.*, **13**, 591–604.
(37) PETCH, N. J. (1968) *Fracture*, (Edited by H. Liebowitz), Academic Press, New York, vol. 1, Ch. 5.
(38) MINTZ, B. (1984) Advances in Fracture Research, Pergamon Press, Oxford, pp. 1247–1254.